JOURNAL OF GEOPHYSICAL RESEARCH, VOL. 101, NO. C6, PAGES 13,975–13,991, JUNE 15, 1996

Dynamics of the East India Coastal Current 1. Analytic solutions forced by interior Ekman pumping and local alongshore winds

D. Shankar[1]

Centre for Mathematical Modelling and Computer Simulation, National Aerospace Laboratories Bangalore, India

J. P. McCreary and W. Han

Oceanographic Center, Nova Southeastern University, Dania, Florida

S. R. Shetye

National Institute of Oceanography, Dona Paula, Goa, India

Abstract. A linear, continuously stratified model is used to investigate how forcing by interior Ekman pumping and local alongshore winds affects the East India Coastal Current (EICC). Solutions are found analytically to an approximate version of the equations of motion. They are obtained in a basin that resembles the actual Bay of Bengal north of 6°N and are forced by *Hellerman and Rosenstein* [1983] winds. The mathematical structure of the solution clearly illustrates the model physics. In response to interior Ekman pumping, baroclinic Rossby waves are excited in the interior of the Bay; they propagate to the western boundary where they generate a northward, coastal current if the interior circulation is anticyclonic and vice versa. In contrast, the response forced by the local alongshore winds is a coastal current that is trapped within the surface mixed layer. Consistent with the observed surface current, the model EICC flows northward along the Indian coast from March to September and equatorward along the Indian and Sri Lankan coasts from October to January. In contrast to the observations, however, the onset of northward flow along the Indian coast occurs 1-2 months late, the Sri Lankan coastal current does not reverse to flow southward during the summer, and the maximum northward transport of the model EICC is 5 Sv in May, only about half the transport estimated from hydrographic data. We conclude that, although interior Ekman pumping and local alongshore winds have a significant impact on the EICC, other driving mechanisms must be taken into account in order to simulate the observed variability adequately.

1. Introduction

Like the Somali Current in the Arabian Sea, the East India Coastal Current (EICC) reverses direction twice a year, flowing northeastward from February until September with a strong peak in March-April and southwestward from October to January with strongest flow in November (see the ship-drift plots in Figure 1). The surface circulation in the interior of the Bay of Bengal is best organized from February to May, when the EICC forms the western boundary current of a basin-wide anticyclonic gyre. Figure 1 does not clearly show the gyre, but it is evident in the seasonal dymamic topography computed from *Levitus* [1982] data [*Shetye et al.*, 1993]; dynamic topography for other seasons does not show a similar basin-wide organization. [*Shetye et al.*, 1991, this issue].

An important driving mechanism of the EICC variability is certainly the winds within the Bay, which also reverse with the monsoons (see Figure 2). However, the peak months of the monsoons (January and July) do not coincide with the times of maximum current speed (March and November), so the relationship between the winds and the currents is not an obvious one. Indeed,

[1]Now at National Institute of Oceanography, Dona Paula, Goa, India.

Paper number 96JC00559.
0148-0227/96/96JC-00559$09.00

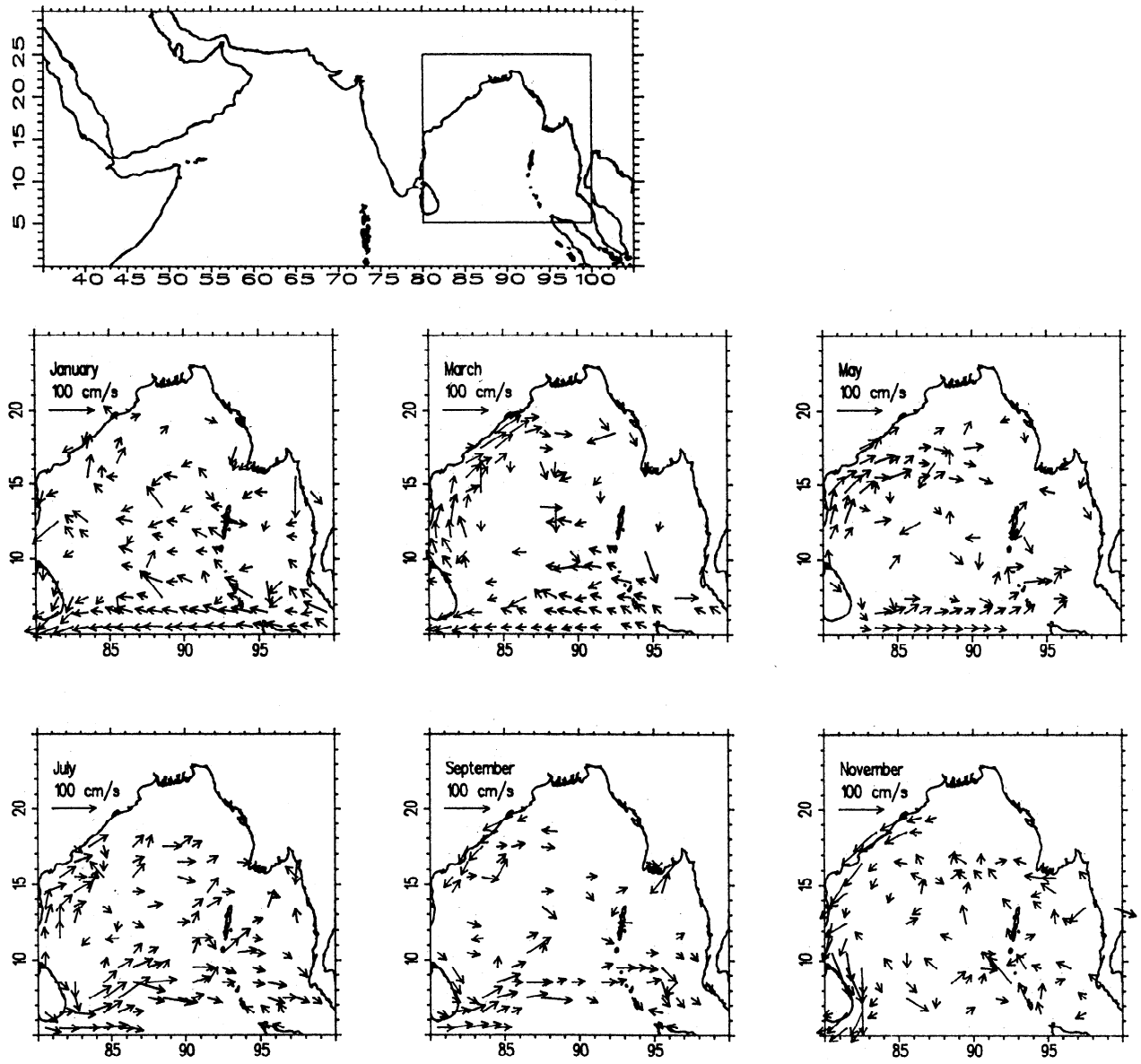

Figure 1. Bimonthly maps of ship-drift vectors [from *Cutler and Swallow*, 1984]. Only current arrows with speeds greater than 20 $cm\,s^{-1}$ are shown. Also shown (top) is the location of the Bay of Bengal in the north Indian Ocean. Off India, the surface EICC flows northeastward from February to September, when it reverses to flow southwestward. Off Sri Lanka, the EICC is southward during most of the year, flowing northward only from February to March.

four different driving mechanisms have been proposed to account for various aspects of the EICC variability. Three of them involve forcing by winds within the Bay: interior Ekman pumping, "local" alongshore winds adjacent to the Indian and Sri Lankan coasts, and "remote" alongshore winds adjacent to the northern and eastern boundaries of the basin. (Throughout this paper we use the phrase "forcing by alongshore winds" to mean "forcing by coastal Ekman pumping," the process in which Ekman flows that converge on or diverge from coasts generate geostrophic currents.) The fourth mechanism invokes remotely forced signals that propagate into the Bay from the equator.

Shetye et al. [1993] proposed that interior Ekman pumping was the primary forcing mechanism of the northeastward EICC from February to May. They noted that the wind-stress curl is negative over most of the Bay at this time (similar to the plots of Ekman pumping velocity in the December, January, and March panels of Figure 2) and that the EICC appears to be the western branch of a large anticyclonic gyre. They therefore hypothesized that the EICC was a northeastward, western boundary current that compensates for southward Sverdrup transport in the interior ocean, as in the barotropic models of *Stommel* [1948] and *Munk* [1950].

McCreary et al. [1993] suggested that forcing by both local and remote alongshore winds also influences the EICC. Local alongshore winds drive an EICC in the direction of the wind. Remote alongshore winds affect the EICC by exciting coastal Kelvin waves that propagate anticlockwise around the perimeter of the Bay, as well as Rossby waves that radiate westward from the eastern boundary. *McCreary et al.* [1993] argued that the collapse of the local alongshore winds at the end of the Southwest Monsoon caused the southwestward EICC in the fall and winter and that remote alongshore winds were responsible for the onset of the northeastward EICC in February.

Yu et al. [1991] and *Potemra et al.* [1991] proposed that remote forcing from the equator could have an important effect within the Bay. In this mechanism, equatorial Kelvin waves reflect off the eastern boundary of the Indian Ocean, partly as a packet of coastal Kelvin waves that propagate around the perimeter of the Bay and partly as a packet of Rossby waves that radiate westward back into its interior. *McCreary et al.* [1993] commented on the relative importance of this process in their solution, suggesting that it was influential primarily during the Southwest Monsoon when it tends to drive southwestward flow in the EICC against the prevailing winds.

In this paper and its companion study [*McCreary et al.*, this issue], we use an ocean model to assess the relative importance of each of the above processes in forcing the EICC. The model is essentially the linear, continuously stratified system of *McCreary* [1980, 1981] in which solutions are found in a realistic basin and forced by climatological winds. In this part of the research we obtain analytic solutions to an approximate version of the equations of motion. The advantage of this approach is that the mathematical structure of the analytic solution clearly reveals the fundamental physics of the system. The approach is limited, however, in that Rossby waves generated along the eastern boundary of the Bay of Bengal cannot be accurately represented (see the end of section 3.1). Consequently, here we consider only effects forced by interior Ekman pumping and local alongshore winds.

2. Model Ocean

2.1. Equations of Motion

The model equations of motion, linearized about a stably stratified background state of no motion, are

$$u_t - fv + \frac{1}{\bar{\rho}}p_x = \tau^x Z(z) + (\nu u_z)_z + \nu_2 \nabla^2 u, \quad (1a)$$

$$v_t + fu + \frac{1}{\bar{\rho}}p_y = \tau^y Z(z) + (\nu v_z)_z + \nu_2 \nabla^2 v, \quad (1b)$$

$$u_x + v_y + w_z = 0, \quad (1c)$$

$$\rho_t - \frac{\bar{\rho} {N_b}^2 w}{g} = (\kappa\rho)_{zz}, \quad (1d)$$

$$p_z = -\rho g, \quad (1e)$$

where u, v, and w are the zonal, meridional, and vertical velocity anomalies, p and ρ are the pressure and density anomalies, g is the acceleration due to gravity, $f = \beta y$ is the Coriolis parameter, $N_b(z)$ is the Brünt-Väisälä frequency associated with the background state, and $\bar{\rho}$ is a typical value for the density of seawater ($\bar{\rho} = 1\ \mathrm{gm\,cm^{-3}}$). The parameters ν and κ are coefficients of vertical eddy viscosity and diffusivity, and ν_2 is the coefficient of Laplacian mixing. The quantities τ^x and τ^y are the zonal and meridional components of the wind stress that force the system, and the stress enters the ocean as body force with the vertical structure $Z(z)$ (see section 2.4).

To permit the representation of solutions as vertical-mode expansions, the mixing coefficients ν and κ, as well as the surface and bottom boundary conditions, must have specific forms that are consistent with (4a) and (4b). The mixing coefficients are

$$\nu = \kappa = \frac{A}{{N_b}^2}. \quad (2)$$

The boundary conditions at the ocean surface ($z = 0$) and the flat bottom ($z = -D$) are

$$\nu u_z = \nu v_z = w = \frac{\rho}{{N_b}^2} = 0. \quad (3)$$

See *McCreary* [1980, 1981] for a discussion of these restrictions.

2.2. Vertical-Mode Expansions

We look for solutions to (1a)-(1e) as expansions in the vertical normal modes of the system. These modes are the eigenfunctions, $\psi_n(z)$, that satisfy

$$\left(\frac{1}{{N_b}^2}\psi_{nz}\right)_z = -\frac{1}{{c_n}^2}\psi_n(z), \quad (4a)$$

subject to boundary conditions

$$\psi_{nz}(-D) = \psi_{nz}(0) = 0. \quad (4b)$$

They form an orthogonal set, are normalized so that

$$\psi_n(0) = 1, \quad (4c)$$

and are ordered so that their eigenvalues c_n decrease monotonically with n. The $n = 0$ eigenfunction is the barotropic mode of the system, and because the ocean surface is a rigid lid, its eigenvalue c_0 is ∞ and $\psi_0(z) = 1$. The eigenfunctions for $n \geq 1$ are the baroclinic modes, and their eigenvalues are finite. Equations (4a) and (4b) then imply that $\int_{-D}^{0} \psi_n dz = 0$ for $n \geq 1$ so that the horizontal transport relative to the ocean bottom associated with each baroclinic mode vanishes.

Appropriate expansions of the model variables are

$$u = \sum_{n=0}^{N} u_n \psi_n, \quad (5a)$$

$$v = \sum_{n=0}^{N} v_n \psi_n, \tag{5b}$$

$$p = \sum_{n=0}^{N} \bar{\rho} p_n \psi_n, \tag{5c}$$

$$w = \sum_{n=0}^{N} w_n \int_{-D}^{z} \psi_n(z')dz', \tag{5d}$$

$$\rho = \sum_{n=0}^{N} \rho_n \psi_{nz}, \tag{5e}$$

where the expansion coefficients are functions of only x, y, and t. The summations should extend to infinity; however, the solutions converge rapidly enough with n for the series to be truncated at a small value of N. The summations also include contributions from the barotropic mode, but in fact solutions are dominated by the baroclinic response (see the end of section 2.4). For convenience, a factor of $1/\bar{\rho}$ is absorbed into the definition of p_n and with this choice p_n has units of velocity squared.

To find the equations for the expansion coefficients, we substitute (5a)–(5c) into (1), multiply (1a)–(1c) by ψ_n, (1d) by ψ_{nz}, (1e) by $\int_{-D}^{z} \psi_n(z')dz'$, and integrate over the water column. After a few integrations by parts and the use of (2)–(4c), it follows that

$$\left(\partial_t + \frac{A}{c_n^2}\right) u_n - f v_n + p_{nx} = F_n + \nu_2 \nabla^2 u_n, \tag{6a}$$

$$\left(\partial_t + \frac{A}{c_n^2}\right) v_n + f u_n + p_{ny} = G_n + \nu_2 \nabla^2 v_n, \tag{6b}$$

$$\left(\partial_t + \frac{A}{c_n^2}\right) \frac{p_n}{{c_n}^2} + u_{nx} + v_{ny} = 0, \tag{6c}$$

$$w_n = \left(\partial_t + \frac{A}{c_n^2}\right) \frac{p_n}{{c_n}^2}, \tag{6d}$$

$$\rho_n = -\frac{p_n}{g}, \tag{6e}$$

where $F_n = \tau^x \mathcal{Z}_n/(\bar{\rho}\mathcal{H}_n)$, $G_n = \tau^y \mathcal{Z}_n/(\bar{\rho}\mathcal{H}_n)$. The factors

$$\mathcal{Z}_n = \int_{-D}^{0} Z(z)\psi_n dz, \quad \mathcal{H}_n = \int_{-D}^{0} {\psi_n}^2 dz \tag{7}$$

determine how strongly the driving wind couples to each mode.

2.3. Lateral Boundary Conditions

Solutions are found in a semienclosed basin that resembles the actual Bay of Bengal (compare the basins in Figures 1 and 2). Its western and northern boundaries represent the coasts of Sri Lanka, India, and Bangladesh; its eastern boundary corresponds to the coasts of Burma, Thailand, and Sumatra; and the southern boundary is an artificial one extending across the basin at 6°N.

Along continental margins it is common to adopt the closed boundary condition that the normal component of the total velocity field vanishes (condition 1). However, to obtain a solution that is forced by interior Ekman pumping alone, we adopt the less stringent boundary condition that only the normal component of the geostrophic flow vanishes (condition 2); this condition allows Ekman flow to pass through the boundary and therefore filters out circulations driven by alongshore winds (i.e., by coastal Ekman pumping). To obtain a solution that includes the response forced by local alongshore winds, we apply condition 1 along the western boundary of the Bay and condition 2 along its northern and eastern boundaries. Our model includes horizontal mixing to be able to solve for the structure of the western boundary current; hence a second boundary constraint is needed, and we utilize the no-slip condition that the tangential component of the velocity equals zero.

An additional condition is needed to specify solutions completely. An application of the principle, solutions are forced only by winds within the Bay (condition 3), is sufficient for this task. Condition 3 ensures that remote forcing from the equator is absent in our model.

2.4. Parameters

The background Brünt-Väisälä frequency, $N_b(z)$, used in the model is the one adopted by *Moore and McCreary* [1990], and the depth of the basin is $D = 4000$ m; corresponding characteristic speeds c_n and coupling factors $\mathcal{H}_n$ are listed in Table 1 for some of the baroclinic modes. The number of modes used is $N = 10$, and with this choice the solution is well converged when $Z(z)$ has the structure (8). The vertical mixing parameter A is 1.3×10^{-4} cm^2 s^{-3}, again as in the *Moore and McCreary* [1990] study, but solutions are not sensitive to its value (see the discussion near the end of section 3.1). Values of β and ν_2 are 2.28×10^{-13} cm^{-1}s^{-1} and 5×10^7 cm^2 s^{-1}, respectively.

The only constraint on the form of the body-force structure $Z(z)$ is that $\int_{-D}^{0} Z(z)dz = 1$, which ensures that the total stress that enters the ocean is the applied wind stress. Typically, in models of this sort, $Z(z) = \theta(z+h)/h$, where θ is a step function. However, with this choice the Ekman-flow part of the response converges very slowly with n because a large number of modes are needed to resolve the jump at the base of the mixed layer. To avoid this problem, we adopt the "smoother" ramped structure

$$Z(z) = \begin{cases} \dfrac{2}{3h}, & -h < z \le 0 \\ \dfrac{2(z+2h)}{3h^2}, & -2h < z \le -h \\ 0, & \text{otherwise,} \end{cases} \tag{8}$$

where $h = 50$ m. The effect of the ramp is that $\mathcal{Z}_n$ values decrease much more quickly with n than they do

Table 1. Values of Various Quantities Associated With Individual Vertical Modes

		Modenumber						
Parameter	Notation	0	1	2	3	4	5	10
Charac. speed	c_n, cm s^{-1}	∞	264	167	105	75	60	30
Mode coupling coeff.	$\mathcal{H}_n$, m	4000	276	171	786	911	1842	4092
Wind coupling coeff.	$\mathcal{Z}_n$	1	0.98	0.96	0.91	0.82	0.74	0.26
Rossby radius	R_n, km	∞	87.0	55.1	34.6	24.7	19.7	9.8
Rossby wave speed	c_{rn}, cm s^{-1}	∞	17.4	6.95	2.73	1.39	0.89	0.22
Rossby wavelength	λ_n, km	∞	5420	2160	848	434	277	69
Decay scale	α_n^{-1}, km	∞	93,600	14,900	2290	599	244	15
Arg. of resp. integral	$\lvert\kappa_n\rvert\mathcal{W}$	0	0.58	1.45	3.71	7.29	11.5	56.8
Amp. of resp. integral	$\lvert\mathcal{I}_n\rvert$, km	500	492	450	234	57	42	8.8
Convergence factor	γ_n	125	1750	2530	269	52	17	0.55

Terms that depend on latitude are evaluated at 12°N, for which the Coriolis parameter f is 3.02×10^{-5} s^{-1}. Terms that depend on frequency are evaluated for $\omega = 2\pi$ yr^{-1}. The length scale for the wind stress $\mathcal{W}$ is taken to be 500 km.

for the step-function profile. Some $\mathcal{Z}_n$ values are listed in Table 1; for comparison the corresponding value of $\mathcal{Z}_{10}$ for the step-function profile is 0.96.

One measure of the strength of an individual mode's response is its coupling coefficient to the wind, $\mathcal{Z}_n/\mathcal{H}_n$. Using the values in Table 1, the ratio $(\mathcal{Z}_0/\mathcal{H}_0)/(\mathcal{Z}_n/\mathcal{H}_n)$ has the values 0.07 and 0.04 for the $n = 1$ and $n = 2$ modes, respectively, and hence the baroclinic response dominates the barotropic one. Thus, although the barotropic contribution is included in all of the fields plotted in this paper, it is negligible for all of them except the barotropic transport field in Figure 8. (A similar conclusion holds for the alternate measure γ_n defined near the end of section 3.1.)

3. Solution

In the first two parts of this section we find an analytic solution to an approximate version of (6a)–(6c) when the forcing is at a single frequency ω. Specifically, we solve for the interior-ocean response in section 3.1 and then obtain the boundary solution required to close the interior circulation in section 3.2. In section 3.3 we write down the general solution for a forcing that contains more than one frequency.

3.1. Interior Response

To derive the approximate set of equations for the interior response, we first define nondimensional variables by

$$(x, y, t, u_n, v_n, p_n, F_n, G_n) = (\mathcal{L}x', \mathcal{L}y', \mathcal{T}t', \mathcal{U}u_n', \mathcal{U}v_n', \mathcal{P}p_n', \mathcal{F}F_n', \mathcal{F}G_n'), \quad (9)$$

so that equations (6a)–(6c) can be rewritten as

$$\left(\frac{1}{f\mathcal{T}}\right) u_{nt}' + \left(\frac{A}{fc_n^2}\right) u_n' - v_n' + \left(\frac{\mathcal{P}}{\mathcal{U}f\mathcal{L}}\right) p_{nx}' = \left(\frac{\mathcal{F}}{f\mathcal{U}}\right) F_n' + \left(\frac{\nu_2}{f\mathcal{L}^2}\right) \nabla^2 u_n', \quad (10a)$$

$$\left(\frac{1}{f\mathcal{T}}\right) v_{nt}' + \left(\frac{A}{fc_n^2}\right) v_n' + u_n' + \left(\frac{\mathcal{P}}{\mathcal{U}f\mathcal{L}}\right) p_{ny}' = \left(\frac{\mathcal{F}}{\mathcal{U}f}\right) G_n' + \left(\frac{\nu_2}{f\mathcal{L}^2}\right) \nabla^2 v_n', \quad (10b)$$

$$\left(\frac{1}{f\mathcal{T}}\right) p_{nt}' + \left(\frac{A}{fc_n^2}\right) p_n' + \left(\frac{\mathcal{U}c_n^2}{\mathcal{P}f\mathcal{L}}\right) (u_{nx}' + v_{ny}') = 0. \quad (10c)$$

Then, with the scalings

$$\frac{\mathcal{P}}{\mathcal{U}f\mathcal{L}} = \frac{\mathcal{F}}{f\mathcal{U}} = 1, \quad (11a)$$

$$\frac{1}{f\mathcal{T}} = \epsilon^2, \quad (11b)$$

$$\frac{\nu_2}{f\mathcal{L}^2} = \epsilon^3, \quad (11c)$$

for all the modes, and the additional scalings

$$\frac{\mathcal{U}c_n^2}{\mathcal{P}f\mathcal{L}} = \frac{A}{fc_n^2} = \epsilon^2 \quad (11d)$$

for the baroclinic modes, where $\epsilon \ll 1$, (10a)–(10c) reduce to the set

$$-fv_n + p_{nx} = F_n, \quad (12a)$$

$$fu_n + p_{ny} = G_n, \quad (12b)$$

$$\left(\partial_t + \frac{A}{c_n^2}\right) \frac{p_n}{c_n^2} + u_{nx} + v_{ny} = 0, \quad (12c)$$

at lowest order. Equations (12a)–(12c) are valid for the barotropic mode, as well as the baroclinic modes, because $c_0 = \infty$ so that the first term of (12c) vanishes. In order to keep track of various physical quantities, (12a)–(12c) and all subsequent equations are written in dimensional variables.

The constraints implied by (11a)–(11d) are all reasonable restrictions in the interior ocean. Equation (11b) states that solutions are valid only when they are slowly varying ($\mathcal{T} \gg f^{-1}$), and this property holds since the wind field forcing the system has periods of 6 months and longer (see section 4.1). The first constraints of (11a) and (11d) imply that the baroclinic solutions are valid only when they are large scale (that is, $\mathcal{L} \gg R_n$, where $R_n \equiv c_n/f$ is the Rossby radius of deformation for the nth mode), which is true in the interior ocean because a typical width scale of the forcing is 500 km or more (Figure 2). (See the end of this section for a further discussion of the validity of this large-scale assumption.) The second constraint of (11d) is a statement that vertical mixing is weak ($A \ll {c_n}^2 f$), and this restriction is easily satisfied for the choice of A and the number of modes N used here. Finally, (11c) is a statement that horizontal mixing is weak ($\nu_2 \ll f\mathcal{L}^2$), which is true for values of ν_2 commonly used in numerical models.

When the term $\left(\partial_t + A/c_n^2\right) p_n/{c_n}^2$ is negligible in (12c), the resulting balance of terms in (12a)–(12c) is the same as the one considered by *Sverdrup* [1947] for the depth-integrated flow field. Hence any mode for which this balance holds is said to be in a state of Sverdrup balance. Since $c_0 = \infty$, the barotropic mode of the system is always in Sverdrup balance. As noted below, however, this term is not at all negligible for the baroclinic modes, and therefore the baroclinic response of the model differs considerably from the idealized Sverdrup state.

Eliminating u_n and v_n from (12a)–(12c) yields

$$p_{nt} - c_{rn} p_{nx} + \left(\frac{A}{{c_n}^2}\right) p_n = -{c_n}^2 \frac{\mathcal{E}\mathcal{Z}_n}{\mathcal{H}_n}, \tag{13}$$

where $c_{rn} = \beta {c_n}^2/f^2$ is the speed of the nth mode Rossby wave, and $\mathcal{E} = [(\tau^y/f)_x - (\tau^x/f)_y]/\bar{\rho}$ is the Ekman pumping velocity. We seek solutions to (13) when $\mathcal{E}$ is a periodic forcing of the form

$$\mathcal{E}(x,y,t) = \phi(x,y)e^{i\omega t}, \tag{14}$$

where ϕ is a complex function that describes the amplitude and phase of a forcing at frequency ω.

With $\mathcal{E}$ given by (14), solutions to (13) can be represented as

$$p_n(x,y,t) = \mathcal{P}_n(x,y)e^{i\omega t}. \tag{15}$$

Substituting (14) and (15) into (13), we obtain

$$\left(i\omega + \frac{A}{{c_n}^2}\right)\mathcal{P}_n - c_{rn}\mathcal{P}_{nx} = -\frac{f^2 c_{rn}}{\beta}\frac{\phi\mathcal{Z}_n}{\mathcal{H}_n}. \tag{16}$$

A Fourier transform in x of (16) then yields

$$\mathcal{F}[\mathcal{P}_n] = -\frac{if^2\mathcal{Z}_n}{\beta\mathcal{H}_n}\frac{\mathcal{F}[\phi]}{k - {c_{rn}}^{-1}(\omega - iA/{c_n}^2)}, \tag{17}$$

where k is the Fourier transform variable and $\mathcal{F}[\mathcal{Q}(x,y)]$ is the Fourier transform of $\mathcal{Q}$.

The inverse transform of (17) can be obtained easily with the aid of the transform pair

$$\frac{\mathcal{F}[\mathcal{Q}]}{k-a} \leftrightarrow ie^{iax}\int_L^x \mathcal{Q}e^{-iax'}dx', \tag{18a}$$

where the lower limit of the integral, $L(y)$, is an unknown function to be determined from boundary conditions 2 and 3 (see section 2.3). Since our basin has an eastern boundary, a more useful form of (18a) is

$$\frac{\mathcal{F}[\mathcal{Q}]}{k-a} \leftrightarrow ie^{iax}\int_{x_e}^x \mathcal{Q}e^{-iax'}dx' + Q(y)e^{ia(x_e - x)}, \tag{18b}$$

where the curve $x_e(y)$ describes the location of the eastern boundary. In (18b) the unknown $L(y)$ has been replaced by an eastern boundary wave of undetermined amplitude $Q(y)$, and boundary conditions 2 and 3 then require that $Q(y) \equiv 0$.

The resulting solution is

$$p_n(x,y,t) = \left[\frac{f^2\mathcal{Z}_n}{\beta\mathcal{H}_n}\int_{x_e}^x \phi(x',y) \cdot e^{-(ik_n+\alpha_n)x'}dx'\right] e^{\alpha_n x}e^{i(k_n x+\omega t)}. \tag{19}$$

The term on the right-hand side describes the generation of Rossby waves with an amplitude given by the term in brackets, their westward propagation with speed c_{rn} and wavenumber $k_n \equiv \omega/c_{rn}$, and their decay due to vertical mixing with the e-folding scale $\alpha_n^{-1} \equiv c_{rn}c_n^2/A$; according to (19), Ekman pumping deepens (shallows) the thermocline in regions where it is negative (positive), generating regions of high (low) pressure that subsequently extend westward due to Rossby-wave propagation. The response to time-independent forcing can be obtained by setting $\omega = 0$ in (19). The barotropic response can be obtained by taking the limit $c_n \to \infty$ so that the exponentials involving k_n and α_n reduce to unity; in this case, $p_0(x,y,t)$ simplifies to the pressure field of a Sverdrup flow, as it should.

With p_n known, all other flow variables follow directly from (12a), (12b), (6d), (6e), and (5). For example, the horizontal-velocity field is

$$u(x,y,z,t) = \sum_{n=0}^{N}\frac{1}{f}(-p_{ny} + G_n)\psi_n(z), \tag{20a}$$

$$v(x,y,z,t) = \sum_{n=0}^{N}\frac{1}{f}(p_{nx} - F_n)\psi_n(z), \tag{20b}$$

and sea level is given by

$$d = \frac{1}{g}\sum_{n=0}^{N} p_n\psi_n(0), \tag{21}$$

where g is the acceleration of gravity. The baroclinic

contribution to d is the dynamic height of the ocean surface relative to the ocean bottom.

The mathematical structure of the integral in solution (19) ensures that p_n decreases rapidly with n. To demonstrate this point, it is sufficient to evaluate the integral when the forcing is the simple "top-hat" function, $\phi = \theta(\frac{1}{4}\mathcal{W}^2 - x^2)$, confined within the region $-\mathcal{W}/2 \le x \le \mathcal{W}/2$. The strength of the response is proportional to the absolute value of the integral $\mathcal{I}_n = e^{\alpha_n x}\int_{\mathcal{W}/2}^{x} e^{-(ik_n+\alpha_n)x'}dx'$ evaluated at $x = -\mathcal{W}/2$, which is

$$|\mathcal{I}_n| = \frac{2}{|\kappa_n|}e^{-\alpha_n\frac{\mathcal{W}}{2}}\left(\sinh^2\alpha_n\frac{\mathcal{W}}{2}\cos^2 k_n\frac{\mathcal{W}}{2} + \cosh^2\alpha_n\frac{\mathcal{W}}{2}\sin^2 k_n\frac{\mathcal{W}}{2}\right)^{1/2}, \quad (22)$$

where $|\kappa_n| = \left(k_n^2 + \alpha_n^2\right)^{1/2}$. According to (22), $|\mathcal{I}_n| = \mathcal{W}$ when $|\kappa_n|\mathcal{W} \ll 2$ and decreases like $1/|\kappa_n|$ when $|\kappa_n|\mathcal{W} > 2$. Values of $|\kappa_n|\mathcal{W}$ and $|\mathcal{I}_n|$ are included in Table 1 for $\mathcal{W} = 500$ km, and for $n \ge 3$ the system is in the regime $|\kappa_n|\mathcal{W} > 2$ for which $|\mathcal{I}_n|$ falls off with n. Physically, the reason for the falloff is that short-scale (or strongly damped) Rossby waves do not couple efficiently to a large-scale wind stress and so cannot be strongly excited.

The combination of factors, $\gamma_n \equiv \mathcal{Z}_n|\mathcal{I}_n|/\mathcal{H}_n$, provides a measure of the overall magnitude of solution (19), and values of γ_n are also included in Table 1. They decrease very rapidly with n, so much so that γ_3 is weaker than γ_2 by almost an order of magnitude. It follows that the contributions of the $n = 1$ and $n = 2$ baroclinic modes dominate the solution. One consequence of this rapid convergence is that currents extend to considerable depths (see section 4.2.3). Another is that the response is not sensitive to the vertical-mixing parameter A; mixing affects the response via the damping coefficient α_n, and it is negligible (i.e., $\alpha_n\mathcal{W} \ll 1$) for the low-order baroclinic modes.

Finally, note that the Rossby-wave wavelength, $\lambda_n = 2\pi/k_n$, decreases indefinitely with n. It would appear, then, that solution (19) breaks down when λ_n becomes of the order of $2\pi R_n$ and the condition $\mathcal{L} \gg R_n$ is no longer valid. Physically, the reason for this breakdown is that because the term v_{nt} is dropped from (12b), there is no critical latitude for Rossby waves above which they no longer exist [*McCreary*, 1980]; a related deficiency is that because u_{nt} is neglected, meridional propagation of Rossby-wave energy is eliminated [*Schopf et al.*, 1981]. However, neither of these distortions is a problem here because solution (19) converges so rapidly with n that it easily satisfies $\mathcal{L} \gg R_n$ for all modes that make an appreciable (i.e., greater than order ϵ) contribution. On the other hand, it is a problem if one attempts to utilize solutions to (12a)–(12c) to obtain the responses forced by remote alongshore winds and equatorial forcing since the Rossby-wave response to these forcings remains appreciable, even at high modenumbers.

3.2. Northern and Western Boundary Layers

The interior flow field defined by (20a)–(20b) will generally have velocity components normal to the northern and western boundaries of the basin. Hence a boundary-layer solution must be added to the solution of the previous section in order to provide sinks (sources) for onshore (offshore) interior flows.

To describe this boundary layer, it is convenient to define a coordinate system (ξ, η) such that the η axis lies along the western and northern boundaries, with η directed northward and/or eastward and ξ directed offshore. Let $\tilde{u}_n$, $\tilde{v}_n$, and $\tilde{p}_n$ be the across-shore velocity, alongshore velocity, and pressure fields of the boundary-layer solution, respectively. We introduce new nondimensional quantities according to

$$(\xi, \eta, \tilde{u}_n, \tilde{v}_n) = (\mathcal{L}_\xi\xi', \mathcal{L}\eta', \mathcal{U}\tilde{u}_n', \mathcal{V}\tilde{v}_n'), \quad (23a)$$

the other definitions being the same as in (9), and adopt the scalings

$$\mathcal{L}_\xi = \epsilon\mathcal{L}, \quad (23b)$$

$$\mathcal{V} = \mathcal{U}/\epsilon. \quad (23c)$$

These scalings are typical boundary-layer assumptions, stating that the boundary layer is narrow and the alongshore current is much stronger than the across-shore flow.

With scalings (23a)–(23c), the homogenous version of (6a)–(6e) expressed in (ξ, η) coordinates reduces to

$$-f\tilde{v}_n + \tilde{p}_{n\xi} = 0, \quad (24a)$$

$$f\tilde{u}_n + \tilde{p}_{n\eta} = \nu_2\tilde{v}_{n\xi\xi}, \quad (24b)$$

$$\tilde{u}_{n\xi} + \tilde{v}_{n\eta} = 0, \quad (24c)$$

at lowest order. An additional assumption, implicit in (24a)–(24c), is that effects of boundary curvature appear at higher order; this is valid, provided the boundary slope changes on a scale larger than the Rossby radius c_n/f [*Clarke*, 1983; *Grimshaw and Allen*, 1988].

It is possible to obtain the transport of the boundary current without solving (24a)–(24c) for the structure of the boundary-layer solution. Integrating (24c) along the boundary and across the current yields

$$\int_0^{\Delta\xi}\tilde{v}_n(\xi, \eta, t)d\xi = \int_{\eta_e}^{\eta}\tilde{u}_n(0, \eta', t)d\eta', \quad (25)$$

where $\Delta\xi$ is the width of the boundary layer and η_e is the end point of the northern boundary, i.e., the point where the northern boundary intersects the eastern boundary (91.5°E, 20°N). By choosing the lower limit of the η' integral to be η_e, we have imposed the condition that the boundary current vanishes at $\eta = \eta_e$, a constraint required by the property that coastally

trapped waves propagate cyclonically around the Bay. Applying condition 1 along the western portion of the boundary and condition 2 along the northern portion yields

$$\tilde{u}_n(0,\eta,t) = \frac{1}{f}p_{n\eta}(0,\eta,t) - \frac{\tau^\eta(0,\eta,t)\mathcal{Z}_n}{\mathcal{H}_n f}\theta(\eta_w - \eta), \tag{26a}$$

where p_n is the interior pressure field (19) expressed here as a function of ξ and η rather than x and y,

$$\tau^\eta = \chi(0,\eta)e^{i\omega t} \tag{26b}$$

is the forcing due to the alongshore wind, θ is a step function, and η_w is the location of the northwest corner of the Bay (87.5°E, 20°N). It follows from (25) that the boundary-current transport relative to an assumed depth of no motion at $z = -H$ is

$$\tilde{V}(\eta,t) = \sum_{n=0}^{N}\left\{\int_{\eta_e}^{\eta}\tilde{u}_n(0,\eta',t)d\eta' \cdot \int_{-H}^{0}[\psi_n(z) - \psi_n(-H)]\,dz.\right\} \tag{27a}$$

Note that the barotropic mode makes no contribution to (27a) since $\psi_0(z) = 1$. The barotropic transport is

$$\tilde{V}_0(\eta,t) = D\int_{\eta_e}^{\eta}\tilde{u}_0(0,\eta',t)d\eta', \tag{27b}$$

where in this case the depth integral extends over the entire water column.

For our purposes, it is also necessary to solve for the structure of the alongshore current along the western boundary. Solving (24a)–(24c) for a single equation in $\tilde{v}_n$ yields

$$\beta'\tilde{v}_n = \nu_2\tilde{v}_{n\xi\xi\xi}, \tag{28}$$

where $\beta' \equiv f_\eta = \beta\cos\phi$, ϕ is the angle between the η axis (the coastline) and the y axis, and we have utilized scaling (23c) to neglect a term $f_\xi\tilde{u}_n$ with respect to $\beta'\tilde{v}_n$. (Although we do not do so here, it is also possible to solve for the boundary layer along the northern boundary. The boundary-layer equation, $\beta\tilde{v}_{n\eta} = \nu_2\tilde{v}_{n\xi\xi\xi\xi}$, holds there, resulting in a boundary layer that broadens to the west like $\eta^{1/4}$.) Applying a no-slip condition at the coast, the solution to equation (28) is the familiar *Munk* [1950] layer,

$$\tilde{v}_n = \mathcal{V}_n(\eta,t)e^{-\gamma\xi}\sin\left(\sqrt{3}\gamma\xi\right), \tag{29}$$

where $\gamma = \frac{1}{2}\sqrt[3]{\beta'/\nu_2}$ and $\mathcal{V}_n$ is an, as yet, unspecified amplitude. Note that solution (29) does not cancel the alongshore current of the interior solution so that the no-slip condition is not completely imposed; however, this error is small because, according to scaling (23c), the cancellation of the interior alongshore flow is an order-ϵ correction to (29).

Integrating (29) across the width of the boundary layer yields

$$\int_0^{\Delta\xi}\tilde{v}_n(\xi,\eta,t)d\xi = \frac{\sqrt{3}}{4\gamma}\mathcal{V}_n, \tag{30}$$

assuming that $\Delta\xi$ is large enough so that contributions from the upper limit are negligible, and with the aid of (25) it then follows that

$$\mathcal{V}_n(\eta,t) = \frac{4\gamma}{\sqrt{3}}\int_{\eta_e}^{\eta}\tilde{u}_n(0,\eta',t)d\eta'. \tag{31}$$

Thus the spatial and temporal structure of the model western boundary current is given by

$$\tilde{v}(\xi,\eta,z,t) = \sum_{n=0}^{N}\mathcal{V}_n(\eta,t)e^{-\gamma\xi}\sin\left(\sqrt{3}\gamma\xi\right)\psi_n(z), \tag{32a}$$

with $\mathcal{V}_n$ provided by (31).

The response to interior Ekman pumping alone $\tilde{v}_{\mathrm{EP}}$ is solution (31) and (32a) when the term proportional to τ^η is dropped from (26a); that is,

$$\tilde{v}_{\mathrm{EP}}(\xi,\eta,z,t) = \sum_{n=0}^{N}\int_{\eta_e}^{\eta}\frac{1}{f}p_{n\eta}(0,\eta',t)d\eta' \cdot \frac{4\gamma}{\sqrt{3}}e^{-\gamma\xi}\sin\left(\sqrt{3}\gamma\xi\right)\psi_n(z). \tag{32b}$$

The convergence of this series is determined by the convergence properties of p_n itself, and therefore the series is dominated by the first two baroclinic modes. Likewise, the response forced only by local alongshore winds, $\tilde{v}_{\mathrm{LA}}$, is obtained by setting $\mathcal{E} = 0$ so that the model is driven only by τ^η south of η_w. It follows from (26a) that $\mathcal{V}_n$ does not depend in any way on c_n. As a result, the summation in (32a) can be evaluated exactly, yielding

$$\tilde{v}_{\mathrm{LA}}(\xi,\eta,z,t) = -\int_{\eta_e}^{\eta}\frac{1}{f}\tau^\eta(0,\eta',t)\theta(\eta_w - \eta')d\eta' \cdot \frac{4\gamma}{\sqrt{3}}e^{-\gamma\xi}\sin(\sqrt{3}\gamma\xi)\,Z(z), \tag{32c}$$

which has the same vertical structure as the assumed body force. It is worth noting that if the term $\tilde{v}_{nt}$ is retained in the equations of motion, Kelvin-wave energy will propagate downward, as well as southward [*Romea and Allen*, 1983]; however, the angle of descent is so shallow at the low frequencies of interest here that energy is still mainly surface trapped, consistent with solution (32c).

3.3. General Solution

The forcing fields, $\mathcal{E}$ and τ^η, for the solutions in section 4 are not pure sinusoidal oscillations but, rather, are general periodic functions at the annual period P that also contain higher harmonics and annual means. As such, they can be written

$$\mathcal{E} = \sum_{j=0}^{J} \mathcal{R}e\left[(\phi_j(x,y)e^{i\omega_j t}\right], \tag{33a}$$

$$\tau^{\eta} = \sum_{j=0}^{J} \mathcal{R}e\left[\chi_j(0,\eta)e^{i\omega_j t}\right], \tag{33b}$$

where $\omega_j = 2\pi j/P$, and the function $\mathcal{R}e(x)$ designates the real part of its argument. In principle, the summations should extend to infinity, but here it is sufficient to truncate the series at a small value of J.

The solution forced by (33a)–(33b) is a linear combination of the single-frequency solutions obtained in sections 3.1 and 3.2. Specifically, let q be any of the fields plotted in Figures 3-8. Then,

$$q = \sum_{j=0}^{J} \mathcal{R}e\left[q_j\right], \tag{34}$$

where q_j is one of solutions (20a), (20b), (21), (27a), (27b), (32a) or (32b) with subscripts j added to the terms ω, φ, and χ.

4. Application to the Bay of Bengal

In this section we report on the solutions that are forced by climatological winds within the Bay. We begin with a description of the forcing (section 4.1), then report solutions that are forced only by interior Ekman pumping and by local alongshore winds (sections 4.2 and 4.3), and end with a discussion of the velocity and transport fields associated with the model EICC.

4.1. Forcing

Forcing for the model is derived from *Hellerman and Rosenstein* [1983] winds. The winds are first linearly interpolated onto a $0.5° \times 0.5°$ grid, and then the functions ϕ_j and χ_j in (33a) and (33b) are obtained by Fourier transforming their time series at each grid point. Because the lowest three frequencies dominate the data, the series are truncated at $J = 2$. Wind-stress vectors, $\boldsymbol{\tau} = (\tau^x, \tau^y)$, composed of the lowest three harmonics, are obtained throughout the basin by similar means.

Figure 2 shows bimonthly plots of $\boldsymbol{\tau}$ and $\mathcal{E}$, and they are very similar to the original fields [see, for example, *McCreary et al.*, this issue, Figure 1]. The $\boldsymbol{\tau}$ field exhibits the following two dominant flow patterns: northeasterly winds from November through February (the Northeast Monsoon) and southwesterly winds from May to September (the Southwest Monsoon). The $\mathcal{E}$ field also exhibits two distinct regimes, being negative throughout most of the Bay from December to April and positive from May to October. In addition to these large-scale features, there are also three localized regions where $|\mathcal{E}|$ is particularly large. There is a maximum of $\mathcal{E}$ off Sri Lanka and southern India from April through December that is most intense during the Southwest Monsoon, when it is associated with a weakening of $|\boldsymbol{\tau}|$ toward the coast. There is a minimum of $\mathcal{E}$ at the southeast corner of the basin from April until November that extends westward as a band of negative $\mathcal{E}$ from June through August. Finally, there is a strong minimum of $\mathcal{E}$ just off Sri Lanka from December through February.

4.2. Solution Forced by Interior Ekman Pumping

Figures 3a, 3b, and 4a illustrate the spatial and temporal structures of the solution forced only by the interior Ekman-pumping field $\mathcal{E}$. Figure 3a provides bimonthly maps of the resulting surface velocity $\mathbf{v}$ and sealevel d fields in the interior of the Bay. Note in Figure 3a that because $\mathbf{v}$ contains Ekman drift, as well as geostrophic currents (see (20a) and (20b)), current vectors are not parallel to isolines of d. Figure 3b is a latitude-time η-t plot of the surface EICC averaged from the coast at $\xi = 0$ to the first zero crossing of the *Munk* [1950] layer at $\xi = \pi/(\sqrt{3}\gamma)$. Figures 4a and 4b show depth-time z-t plots of the EICC at $\eta = 16°$N, 12°N, and 8°N and at $\xi = \xi_{\max} \equiv \pi/(3\sqrt{3}\gamma)$, the location offshore where the Munk layer attains its maximum value. Figures 3b, 4a, and 4b contain contributions from both the interior and boundary solutions.

4.2.1. Northward EICC. In the northern Bay (north of about 14°N) a region of positive d appears near the eastern basin in November in response to the negative $\mathcal{E}$ field there (Figures 2 and 3a). By January, there is a closed region of high d in the north-central basin, with geostrophic currents circulating anticyclonically about it. From February to April this region strengthens due to local forcing and shifts westward via Rossby-wave propagation, and during May it is a prominent feature in the northwestern basin (Figure 3a, March and May). Thereafter, it weakens due to forcing by positive $\mathcal{E}$, and in July only a small remnant remains. Northeastward flow in the EICC north of 14°N is clearly the western boundary response to this interior circulation; it begins when the anticyclonic gyre meets the western boundary in February, attains its peak strength in May, and continues until July (Figures 3b and 4a, top).

In the southern Bay, regions of positive d driven by negative $\mathcal{E}$ also appear in the eastern basin in November, intensify and propagate westward during the winter (Figures 2 and 3a, November–March), and generate northward flow in the EICC when they reach the western boundary in the spring (Figures 3b and 4a, middle and bottom). In April, however, positive $\mathcal{E}$ begins to decrease d in the southern Bay, and by May the region of positive d exists only in a band of increased d in the western basin near 12°N (Figures 2 and 3a). By July, only a portion of this band in the central basin remains positive, where it is reinforced by the small region of negative $\mathcal{E}$ centered about 90°E, 12°N, but it persists

as a region where d has a relative maximum until October (Figure 3a, September). Because of the decrease in positive d, northward flow in the EICC is absent from the Sri Lankan coast by mid-April and from the southern Indian coast by the end of May (Figures 3b and 4a, middle and bottom). Note in Figure 3b that the pattern of northward flow is quite different south of 8°N than it is farther north, beginning earlier in November and reaching a maximum value during February; this difference is due to forcing by strong negative $\mathcal{E}$ in the

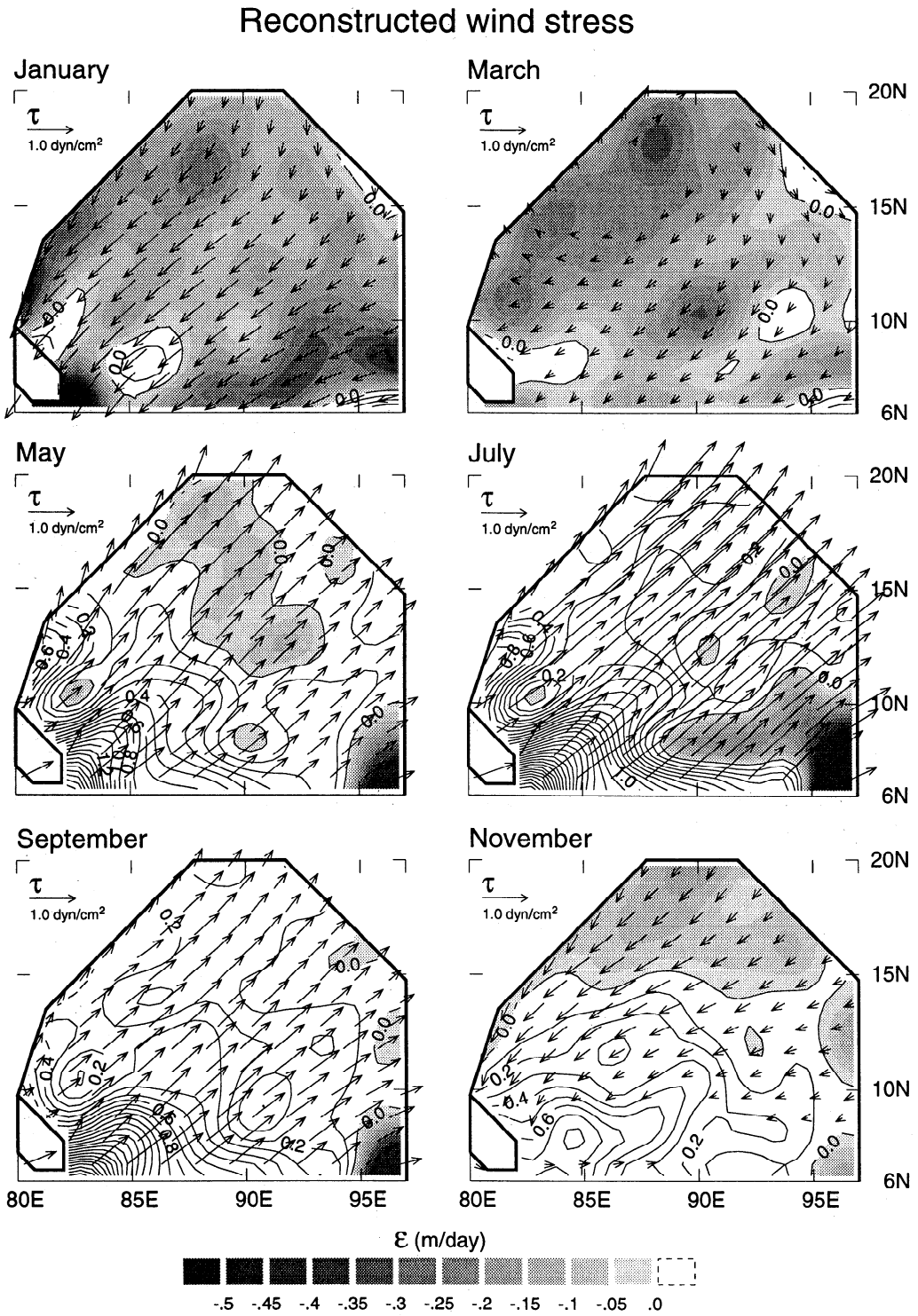

Figure 2. Bimonthly maps of wind-stress vectors τ and Ekman pumping velocity $\mathcal{E}$ derived from the *Hellerman and Rosenstein* [1983] winds. The fields are a superposition of the mean, semiannual, and annual harmonics and closely resemble the original fields. Contour intervals for $\mathcal{E}$ are 0.1 m d^{-1} for positive values and 0.05 m d^{-1} for negative values; negative values are indicated with a graduated gray scale.

localized region present just off Sri Lanka from December to February (Figure 2, January).

4.2.2. Southward EICC. In the northern Bay, $\mathcal{E}$ first becomes positive in a small region adjacent to the eastern boundary during December, and it subsequently intensifies and spreads westward (Figure 2, January–July). In response, a region of negative d appears in the northeastern basin in January, intensifies,

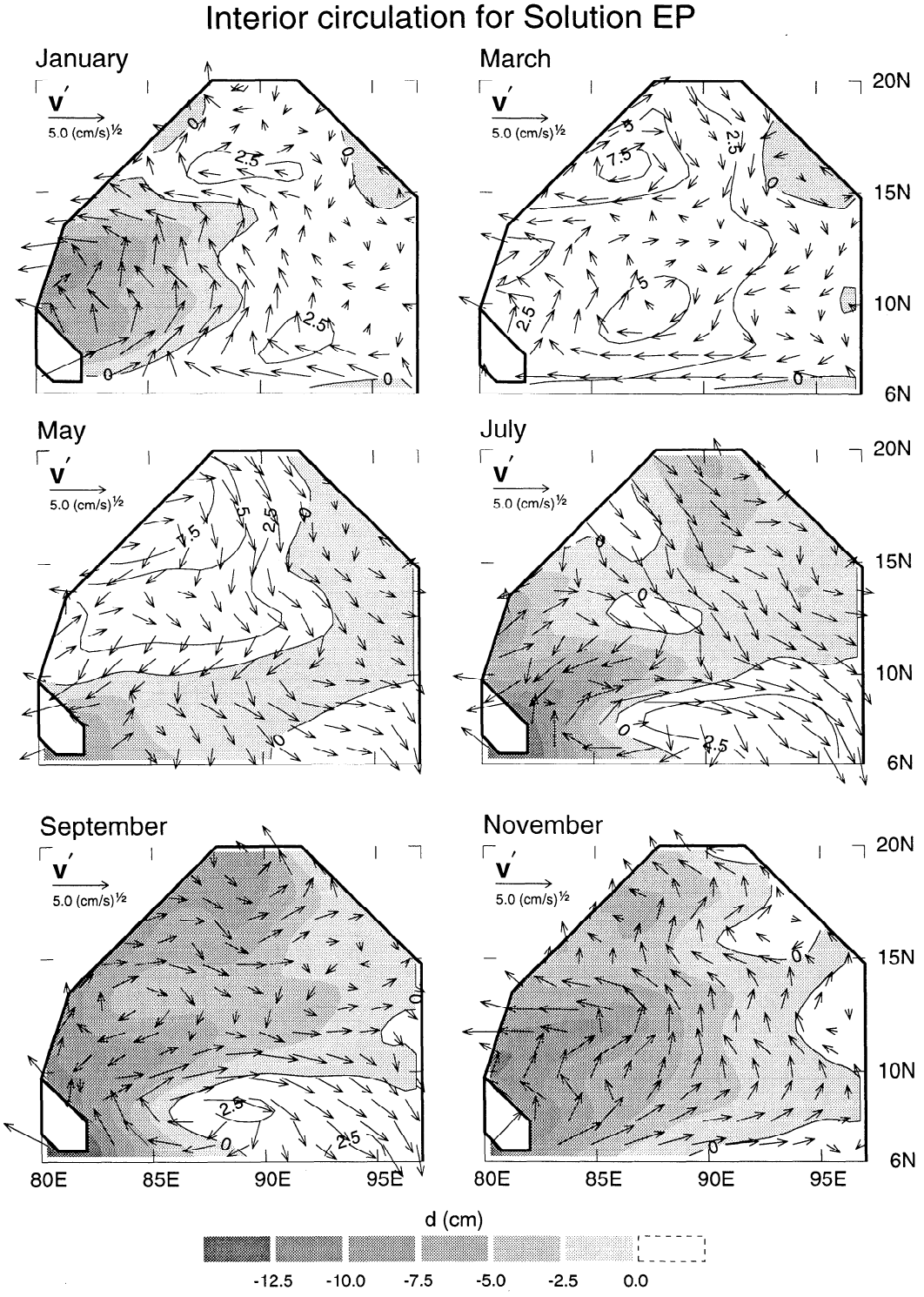

Figure 3a. Bimonthly maps of surface currents $\mathbf{v}$ and sea level d for the interior solution. The fields are determined from solutions (20a), (20b), and (21), as prescribed by (34). The contour interval for d is 2.5 cm, and negative values are indicated with a graduated gray scale. The current arrows are of the vector field $\mathbf{v}' = \mathbf{v}/|\mathbf{v}|^{1/2}$, which has the same direction as $\mathbf{v}$ but an amplitude of $|\mathbf{v}|^{1/2}$; this modification enhances the strength of weak flows relative to stronger ones, allowing them to be more visible in the plots. Current arrows are not parallel to isolines of d because $\mathbf{v}$ contains both Ekman and geostrophic flows.

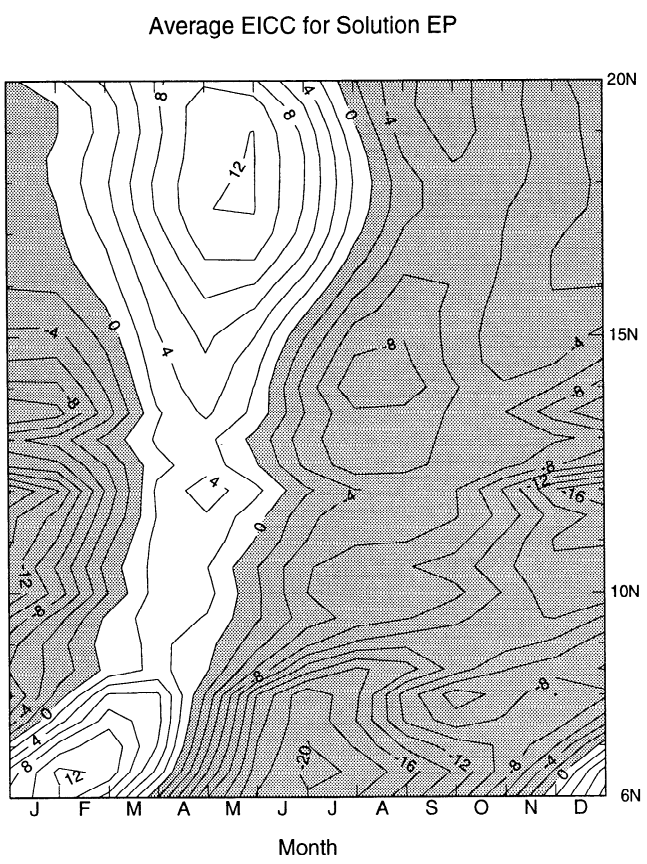

Figure 3b. Latitude-time plot of the average EICC surface flow forced by interior Ekman pumping. The plotted field is determined from the sum of solution (32b) and the alongshore current of interior solution (20a) and (20b), averaged from $\xi = 0$ to $\xi = \pi/(\sqrt{3}\gamma)$ and summed over the lowest three harmonics, as prescribed by (34).

and shifts westward across the basin due partly to the change in location of the forcing and partly to Rossby-wave propagation (Figure 3a). The EICC begins to flow southward in July and August when this negative-d region arrives at the coast, and southward flow continues until the arrival of the positive-d region in the spring (Figures 3b and 4a, top, and section 4.2.1).

In the southern Bay, positive $\mathcal{E}$ in the southwestern basin generates a region of negative d off Sri Lanka in April that expands eastward and strengthens until August, when it covers the entire southwestern portion of the basin (Figures 2 and 3a, May and July). Note the similarity between the horizontal distributions of $\mathcal{E}$ and d in July, a property that clearly indicates the causal relationship between the two fields. The July sea level pattern remains relatively unchanged from September to December, when it begins to shrink due to the weakening of $\mathcal{E}$ and to the positive-d Rossby waves propagating from the east (section 4.2.1). The EICC flows southward wherever the negative-d region hugs the coast (Figures 3b and 4a, middle and bottom).

The localized region of negative $\mathcal{E}$ in the southeastern bay (Figure 2, May–November) generates a band of

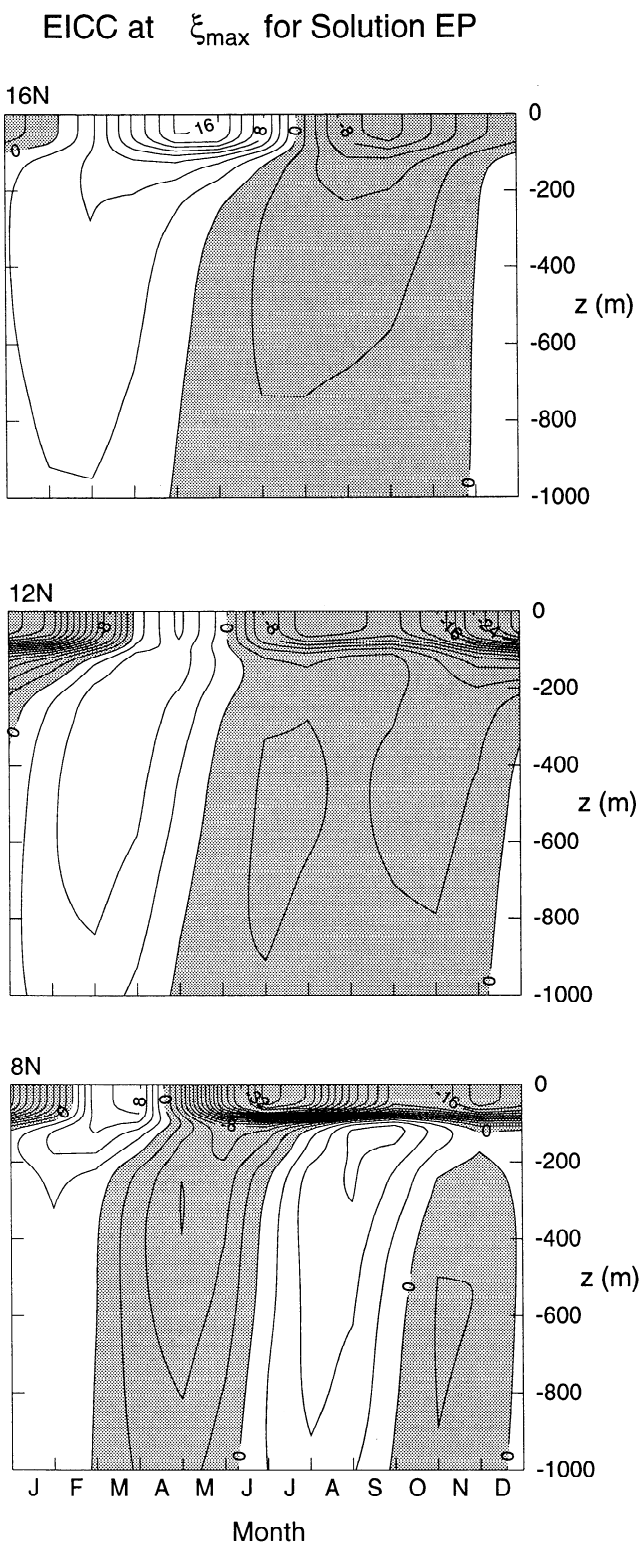

Figure 4a. Depth-time plots of EICC surface flow forced only by interior Ekman pumping at 16°N, 12°N, and 8°N. The plotted field is determined from the sum of solution (32b) and the alongshore current of interior solution (20a) and (20b), evaluated at $\xi = \xi_{max} = \pi/(3\sqrt{3}\gamma)$ and summed over the lowest three harmonics, as prescribed by (34). The contour interval is 2 cm s^{-1}, and regions of southward flow are shaded. The currents extend into the deep ocean, and phase tends to propagate upward.

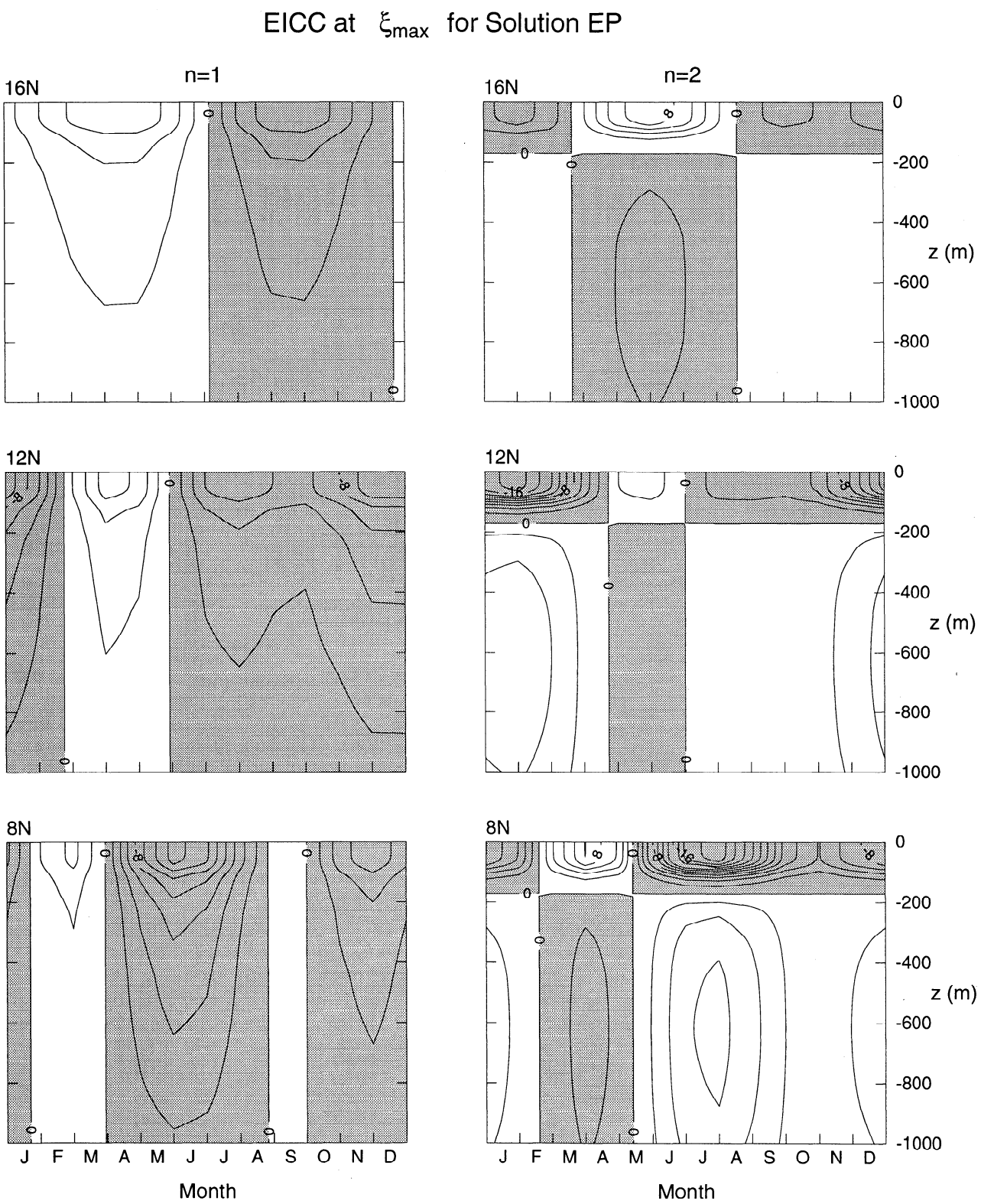

Figure 4b. Same as Figure 4a, except showing the contributions of the (left) $n = 1$ and (right) $n = 2$ baroclinic modes. Currents associated with the $n = 2$ mode change sign near a depth of 170 m and are delayed relative to those of the $n = 1$ mode.

positive d there that extends across much of the basin during the summer (Figure 3a, May–September). Owing to Rossby-wave propagation, the influence of this band actually extends into the western basin, where it makes d less negative. The weakening of southward flow in the EICC that begins in July south of 8°N is traceable to the arrival of this positive-d Rossby wave (Figures 3b and 4a, bottom).

4.2.3. Vertical structure. A striking property of the EICC vertical structure is that the flow field extends to considerable depths (Figure 4a), a result of the interior flow field being dominated by the lowest two baroclinic modes (see the end of section 3.1). In spite of this dominance, the processes that drive the deep flows are not obvious in Figure 4a. For example, just what aspect of the surface wind field drives the deep, southward and northward currents at 8°N during the spring and summer? To help identify the processes, the individual contributions of the $n = 1$ and $n = 2$ modes are plotted in Figure 4b. A comparison of Figures 4a and 4b illustrates visually that the total flow field is primarily an interference pattern between the two contributions.

In the mode-1 response the influence of forcing by large-scale, negative $\mathcal{E}$ is indicated by bands of positive flow from December until July at 16°N, from March through April at 12°N, and during February and March at 8°N; conversely, the influence of large-scale positive $\mathcal{E}$ is indicated by negative flow at other times of the year. The band of weak, positive current during September at 8°N is due to the Rossby wave excited by the localized region of negative $\mathcal{E}$ in the southeastern basin, and its influence is felt from June until November (Figures 2 and 3a, May–November). Similarly, the relative minimum of southward flow during September at 12°N results from the Rossby wave generated by relatively weak or negative $\mathcal{E}$ in the central basin (Figures 2 and 3a, July and September). Analogous features are also visible in the mode-2 solution, but they occur later in the year due to the slower propagation speeds of $n = 2$ Rossby waves (Table 1) and they are associated with a current reversal near a depth of 170 m.

With the aid of Figure 4b it is possible to answer questions like the one posed above. Interestingly, both the southward and northward deep flows at 8°N are driven primarily by the same mechanism, namely, positive $\mathcal{E}$ in the southern Bay. The northward flow is the mode-2 part of the response to this forcing, and it is visible in the total field because of the time lag between the mode-1 and mode-2 contributions. Another noteworthy feature of the total flow field is that isotachs are almost always tilted in such a way that phase propagates upward in time, an indicator that Rossby-wave energy is radiating downward, as well as westward; this property clearly results from the time lag between the two contributions and from the change in sign of the mode-2 solution at depth.

4.3. Solution Forced by Local Alongshore Winds

Figures 5 and 6, analogous to Figures 3b and 4a, illustrate the structure of the solution forced only by the alongshore wind field τ^η. Consistent with the integrand of solution (32c) being proportional to τ^η, the alongshore flow closely follows the local winds, flowing northward during the Southwest Monsoon with a peak value in July and southward during the Northeast Monsoon with a peak value in December (Figure 5). Owing to the integral in (32c) proceeding from north to south (from η_w to η), the strength of the current generally increases southward, the only exception being the slight amplitude decrease from 8°N to 9°N in July (Figure 5) due to τ^η having a weak, downwelling-favorable component along the northeast coast of Sri Lanka (Figure 2, July). Finally, according to (32c), the flow field has the same vertical structure as the body force $Z(z)$ and so is trapped to the surface mixed layer (Figure 6).

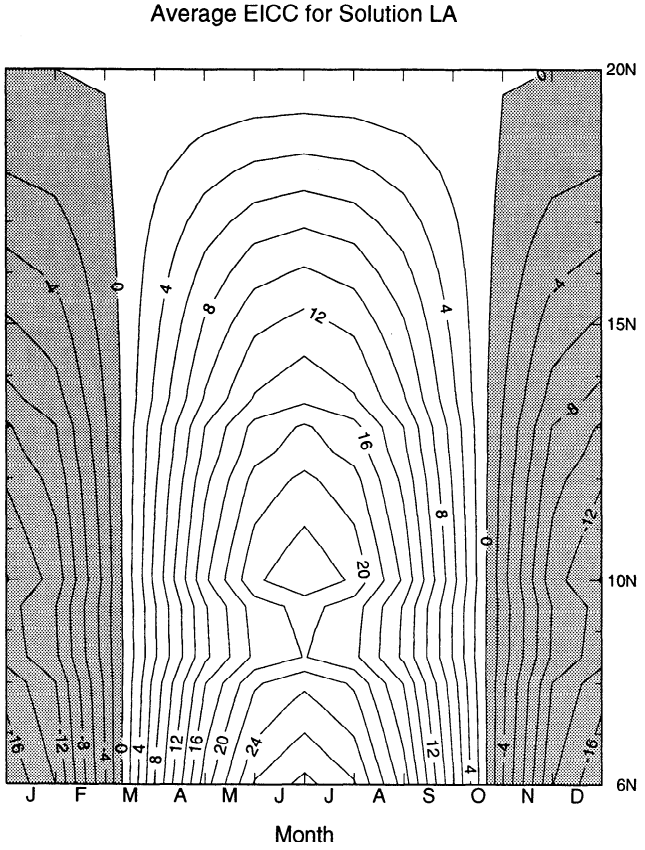

Figure 5. Latitude-time plot of the average EICC surface flow forced only by local alongshore winds. The plotted field is determined from solution (32c), as prescribed by (34). The amplitude of the surface EICC closely follows that of the alongshore wind, and it increases to the south everywhere, except near 9°N during the summer when the winds are downwelling favorable.

4.4. EICC Velocity and Transport

Figure 7 presents time plots of the average surface EICC at 16°N, 12°N, and 8°N due to Ekman pumping only (curves labelled EP), to local alongshore winds alone (curves labelled LA), and to both mechanisms (curves labelled MR). A comparison of the three curves allows the influence of each process on the EICC to be assessed quantitatively. Clearly, northward flow in the EICC is caused primarily by local alongshore winds (LA), with Ekman pumping also contributing to the onset of northward flow at 16°N (EP). Wintertime south-

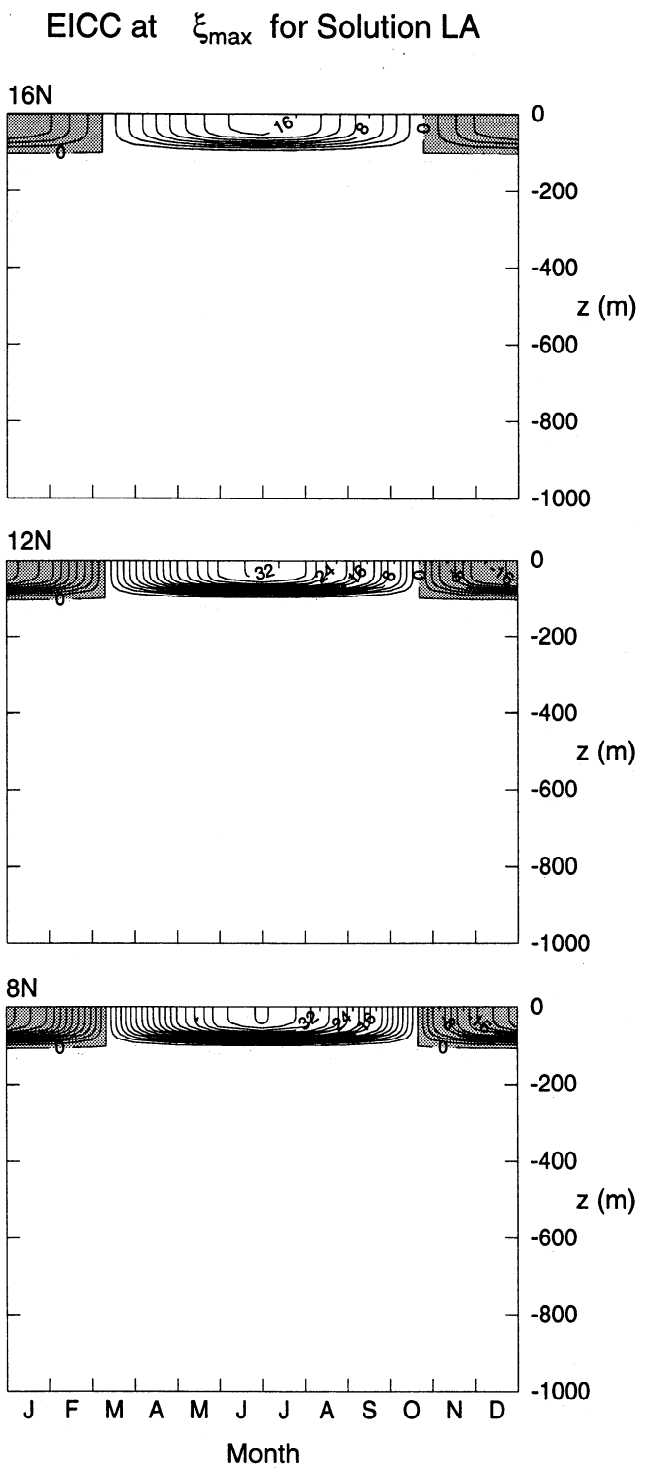

Figure 6. Depth-time plots of EICC flow forced only by local alongshore winds at 16°N, 12°N, and 8°N. The fields are determined from solution (32c), evaluated at $\xi = \xi_{max} = \pi/(3\sqrt{3}\gamma)$, as prescribed by (34). The response is trapped within the surface mixed layer.

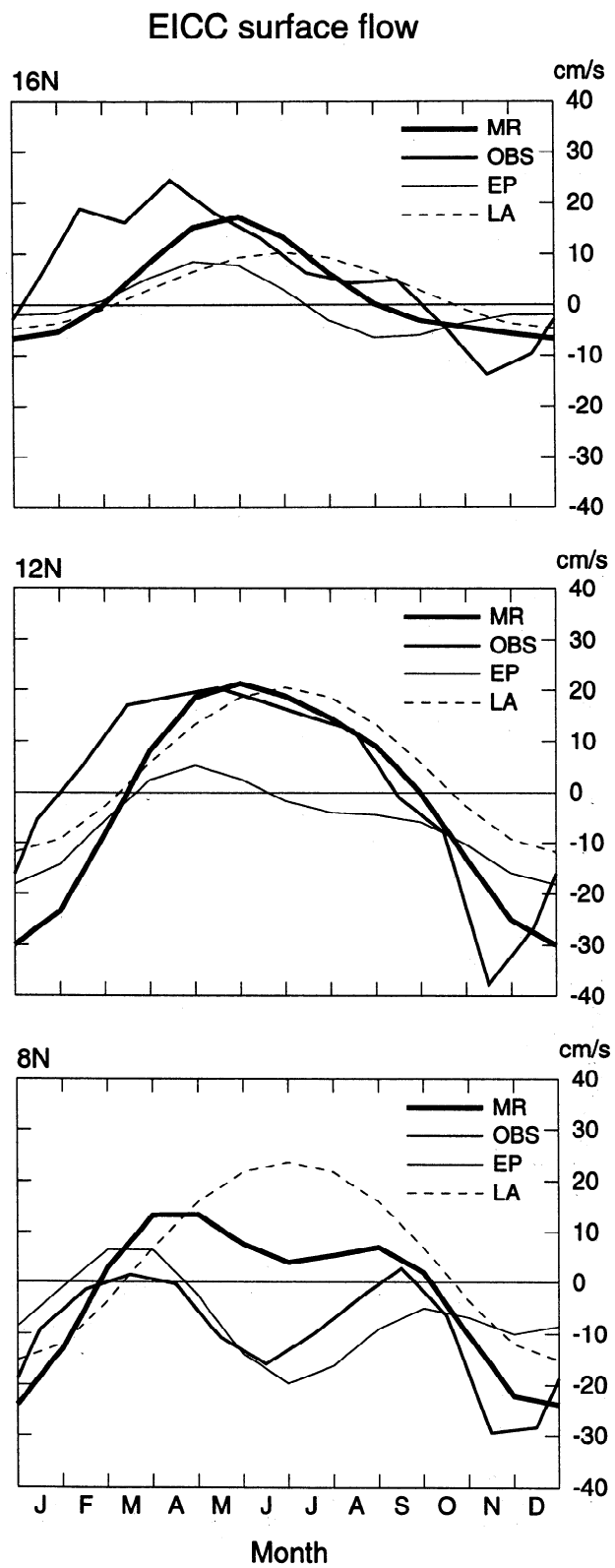

Figure 7. Time plots of the EICC surface flow at 16°N, 12°N, and 8°N, showing the total model response (MR), the response forced only by Ekman pumping (EP), the response forced only by local alongshore winds (LA), and the alongshore flow determined from ship-drift data (OBS). The plotted fields are determined as described in Figures 3b and 5. The onset of northward flow in the model occurs too late along the coast of India. The model EICC flows northward during the summer, whereas the observed current is directed southward.

ward flow is forced roughly equally by Ekman pumping and by alongshore winds. At 8°N, summertime southward flow driven by Ekman pumping is not quite strong enough to overcome the strong northward flow due to the alongshore winds, and so the total current continues to flow northward.

Figure 7 also includes the average EICC determined from the ship-drift data compiled by *Rao et al.* [1989, 1991] (curves labelled OBS). Along the Indian coast (Figure 7, top and middle) the model EICC (MR) agrees well with the data from June to December. However, there is a discrepancy between the two curves from January to May, with the onset of the northward flow occurring more than a month later in the model than it does in the observed flow. Along the Sri Lankan coast, southward flow in the model EICC from October to February compares favorably with the ship-drift data, but it continues to flow northward from March to August, opposite to the direction of the observed flow.

Figure 8 shows time plots of EICC baroclinic transports relative to a depth of no motion at 1000 m (curves labelled MR) and barotropic transports (curves labelled BT) at 16°N, 12°N, and 8°N. The baroclinic transports generally follow their counterparts in Figure 4a, except at 8°N during May to July, when the transport reverses direction due to the presence of deep southward flow (Figure 4a). The obvious difference between curves MR and BT visually demonstrates just how far the baroclinic flow field is from an idealized Sverdrup balance (a result of the slow propagation speeds of baroclinic Rossby waves). Model transport values tend to be less than those estimated from hydrographic data. For example, the maximum northward transport attained in the model is 5 Sv at 16°N during May (MR), considerably less than the value of 10 Sv from hydrographic data [*Shetye et al.*, 1993]. The model's maximum southward transport is 6.7 Sv at 11°N during December, close to but less than the value of 7.7 Sv calculated from data [*Shetye et al.*, this issue].

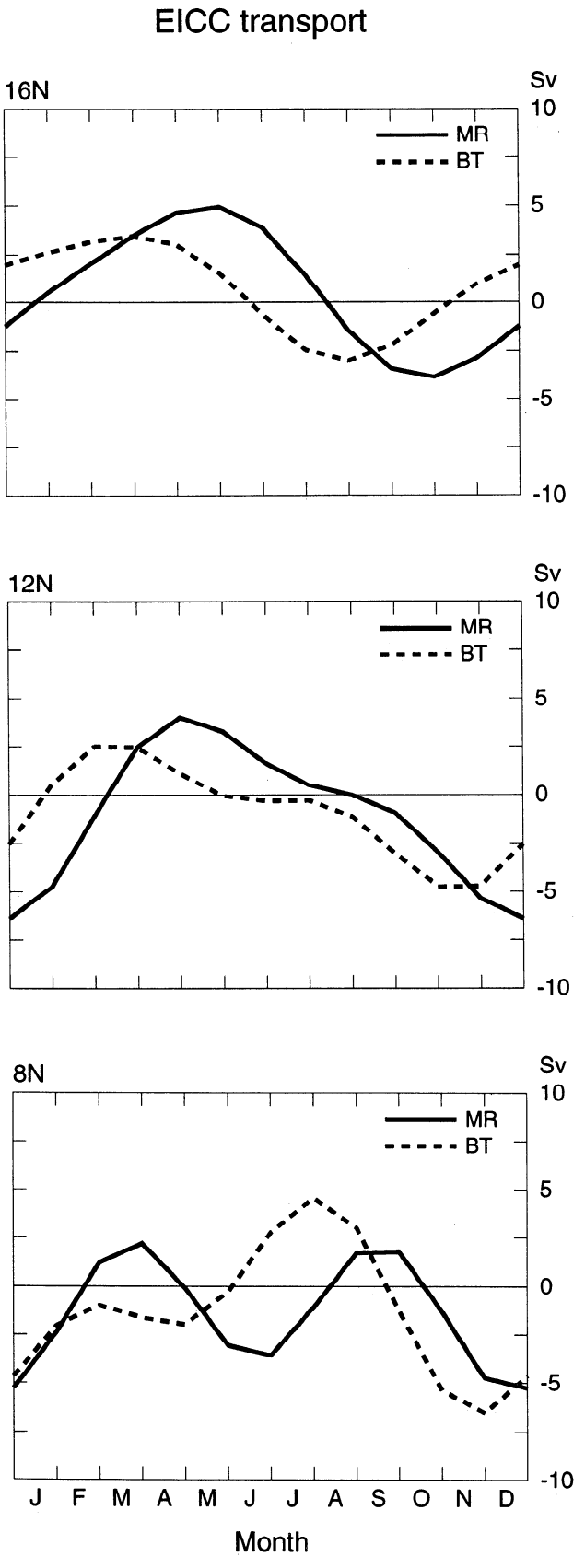

Figure 8. Time plots of the baroclinic (MR) and barotropic (BT) transports at 16°N, 12°N, and 8°N. The transports are determined from (27a) and (27b), as prescribed by (34). The difference between the baroclinic and barotropic curves illustrates how far the baroclinic flow field is from a state of Sverdrup balance.

5. Summary

In this study we have used a linear, continuously stratified model to investigate the dynamics of the EICC forced by interior Ekman pumping and local alongshore winds. Solutions are found analytically to an approximate version of the equations of motion that is valid when the forcing is large scale ($\mathcal{L} \gg c_n/f$) and slowly varying ($T \gg f^{-1}$). They are obtained in a basin that resembles the real Bay of Bengal, and the forcing is a summation of the mean, annual, and semiannual harmonics of the *Hellerman and Rosenstein* [1983] winds. To isolate effects due to Ekman pumping in the interior of the Bay, we apply the boundary conditions that only the normal component of the interior geostrophic flow is cancelled at the continental margins and that the pressure at the southeast corner of the basin vanishes. To include effects due to local alongshore winds, we adopt the preceding conditions and also require that the normal component of the Ekman drift is cancelled along the east coasts of India and Sri Lanka.

In response to forcing by a region of positive (negative) Ekman-pumping velocity $\mathcal{E}$ in the interior of the Bay, Rossby waves with a negative (positive) surface pressure field are generated and propagate westward

(see (19), and Figures 2 and 3a). When these waves arrive at the western boundary, they generate a coastal current, which in our system is a modified *Munk* [1950] layer (see (29)). The amplitude of the current $\mathcal{V}_n$ is determined by an integral that extends from north to south along the boundary, consistent with the propagation direction of coastally trapped waves (see (31)). The $n = 1$ and $n = 2$ modes dominate the response because the wavelengths of higher-order Rossby waves are too short to couple efficiently to the large-scale wind field (see (22)), and as a result, currents driven by $\mathcal{E}$ extend to considerable depths (Figure 4a). Furthermore, delays in the arrival of $n = 2$ Rossby waves at the coast (Figure 4b) cause phase to propagate upward (Figure 4a), an indicator that energy is propagating downward. In contrast, the response to forcing by local alongshore winds is much simpler; it is confined entirely to the western boundary layer, its amplitude is proportional to a coastal integral of τ^η, and it is trapped within the surface mixed layer (see (32c) and Figure 6).

Along the Indian coast the model surface EICC is in good agreement with the ship-drift data from June to December, but the onset of northward flow is delayed by several months in the spring (Figure 7, top and middle) and the maximum northward transport is only 5 Sv, about half the value estimated from hydrographic data. Along the Sri Lankan coast, the model EICC flows southward from October through February, in good agreement with the observations, but it flows northward during the summer, contrary to the data (Figure 7, bottom). We conclude that although Ekman pumping and local alongshore winds are important forcing mechanisms for the EICC, other processes must also be involved. Investigating the influence of the other two processes mentioned in the introduction (remote alongshore winds and equatorial forcing) is the subject of the second part of this research [*McCreary et al.*, this issue].

Acknowledgments. D. Shankar and Satish Shetye were supported by funds from the Department of Ocean Development. Julian McCreary and Weiqing Han were supported by ONR contract N00014-90-J-1054 and by NSF grant OCE-92-03916. We thank Kevin Kohler for his programming assistance, G. S. Michael for the preparation of Figure 1, and P. N. Vinayachandran for several useful discussions.

References

Clarke, A. J., The reflection of equatorial waves from oceanic boundaries, *J. Phys. Oceanogr., 13*, 1193-1207, 1983.

Cutler, A. N., and J. C. Swallow, Surface currents of the Indian Ocean (to 25°S, 100°E), *Tech. Rep. 187*, 8 pp., Inst. of Oceanogr. Sci., Wormley, England, 1984.

Grimshaw, R., and J. S. Allen, Low-frequency baroclinic waves off coastal boundaries, *J. Phys. Oceanogr., 18*, 1124-1143, 1988.

Hellerman, S., and M. Rosenstein, Normal wind stress over the world ocean with error estimates, *J. Phys. Oceanogr., 13*, 1093-1104, 1983.

Levitus, S., Climatological atlas of the world ocean, *NOAA Prof. Pap. 13*, 173 pp., U. S. Govt. Print. Off., Washington, D. C., 1982.

McCreary, J. P., Modelling wind-driven ocean circulation, *Tech. Rep. HIG-80-3*, 64 pp., Hawaii Inst. of Geophys., Honolulu, 1980.

McCreary, J. P., A linear stratified ocean model of the coastal undercurrent, *Philos. Trans. R. Soc. London A, 302*, 385-413, 1981.

McCreary, J. P., P. K. Kundu, and R. L. Molinari, A numerical investigation of dynamics, thermodynamics, and mixed layer processes in the Indian Ocean, *Prog. Oceanogr., 31*, 181-224, 1993. (Correction, *Prog. Oceanogr., 33*, after pg. 248, 1994.)

McCreary, J. P., W. Han, D. Shankar, and S. R. Shetye, Dynamics of the East India Coastal Current, 2, Numerical solutions, *J. Geophys. Res.*, this issue.

Moore, D. W., and J. P. McCreary, Excitation of intermediate frequency equatorial waves at a western ocean boundary: With application to observations from the Indian Ocean, *J. Geophys. Res., 95*, 5192-5231, 1990.

Munk, W. H., On the wind-driven ocean circulation, *J. Meteorol., 7*, 79-93, 1950.

Potemra, J. T., M. E. Luther, and J. J. O'Brien, The seasonal circulation of the upper ocean in the Bay of Bengal, *J. Geophys. Res., 96*, 12,667-12,683, 1991.

Rao, R. R., R. L. Molinari, and J. F. Festa, Evolution of the climatological near-surface thermal structure of the tropical Indian Ocean, 1, Description of mean monthly mixed-layer depth and sea-surface temperature, surface-current, and surface meteorological fields, *J. Geophys. Res., 94*, 10,801–19,815, 1989.

Rao, R. R., R. L. Molinari, and J. F. Festa, Surface meteorological and near-surface oceanographic atlas of the tropical Indian Ocean, *NOAA Tech. Memo. ERL AOML-69*, NOAA Atl. Oceanogr. and Meteorol. Lab., Miami, Fla., 1991.

Romea, R. D., and J. S. Allen, On vertically propagating coastal Kelvin waves at low latitudes, *J. Phys. Oceanogr., 13*, 1241–1254, 1983.

Schopf, P. S., D. L. T. Anderson, and R. Smith, Beta-dispersion of low-frequency Rossby waves, *Dyn. Atmos. Oceans, 5*, 187-214, 1981.

Shetye, S. R., S. S. C. Shenoi, A. D. Gouveia, G. S. Michael, D. Sundar, and G. Nampoothiri, Wind-driven coastal upwelling along the western boundary of the Bay of Bengal during the Southwest Monsoon, *Cont. Shelf Res., 11*, 1397-1408, 1991.

Shetye, S. R., A. D. Gouveia, S. S. C. Shenoi, D. Sundar, G. S. Michael, and G. Nampoothiri, The western boundary current of the seasonal subtropical gyre in the Bay of Bengal, *J. Geophys. Res., 98*, 945-954, 1993.

Shetye, S. R., A. D. Gouveia, D. Shankar, S. S. C. Shenoi, P. N. Vinayachandran, D. Sundar, G. S. Michael, and G. Nampoothiri, Hydrography and circulation in the western Bay of Bengal during the Northeast Monsoon, *J. Geophys. Res.*, this issue.

Stommel, H., The westward intensification of wind-driven ocean currents, *EOS Trans. AGU, 29*(2), 202-206, 1948.

Sverdrup, H. U., Wind-driven currents in a baroclinic ocean; with application to the equatorial currents of the eastern Pacific, *Proc. Natl. Acad. Sci. USA, 33*, 318-326, 1947.

Yu, L., J. J. O'Brien, and J. Yang, On the remote forcing of the circulation in the Bay of Bengal, *J. Geophys. Res., 96*, 20,449-20,454, 1991.

D. Shankar and S. R. Shetye, National Institute of Oceanography, P. O. Box NIO, Dona Paula, Goa 403 004, India. (e-mail: shetye@bcgoa.ernet.in)

W. Han and J. P. McCreary, Oceanographic Center, Nova Southeastern University, 8000 N. Ocean Dr., Dania, FL 33004. (e-mail: jay@ocean.nova.edu)

(Received August 7, 1995; revised January 3, 1996; accepted January 24, 1996.)